of proteins and chemicals including components of cigarette smoke bind to the broad surface area of asbestos.[5] This might result in the accumulation of hazardous molecules.

The first hypothesis stresses the importance of local iron overload in the carcinogenic process of mesothelioma. In 1989, we succeeded in producing a rat model of peritoneal mesothelioma using ferric saccharate followed by administration of an iron chelator, nitrilotriacetate. This model demonstrated, for the first time, that local iron deposition is an important factor in the generation of diffuse malignant mesothelioma.[8] In this study, we have applied two microarray techniques to these iron-induced peritoneal mesotheliomas to elucidate the molecular mechanisms of iron-induced mesothelial carcinogenesis.

MATERIALS AND METHODS

Animal Experiments and Chemicals

The carcinogenesis study was performed as previously described[8] with slight modification, using specific pathogen-free F1 hybrid rats crossed between Fischer344 (F344; female) and Brown-Norway (BN/CIJ; male) strains (Charles River, Yokohama, Japan). In some acute and subacute experiments, specific pathogen-free male Wistar rats (Shizuoka Laboratory Animal Center, Shizuoka, Japan) were also used. Animals were fed a basal diet (Funabashi F-1; Funabashi, Chiba, Japan) and tap water *ad libitum*. Ferric saccharate (Fesin; Yoshitomi Pharmaceutical Company, Osaka, Japan) was prepared in a 5% glucose solution. The nitrilotriacetic acid (NTA) solution was prepared by dissolving NTA, disodium salt (Nakalai Tesque, Kyoto, Japan), in physiological saline, and the pH was adjusted using sodium bicarbonate to pH 7.4. For the carcinogenesis study, a total of 92 F1 hybrid rats were divided into two groups of untreated control ($N=38$) and iron-treated ($N=54$). The injections were started at 4 weeks of age. Ferric saccharate (5 mg iron/kg body weight) was injected intraperitoneally 5 days a week for 12 weeks. NTA (80 mg/kg body weight) was administered separately intraperitoneally 5 days a week for 20 weeks. This form of iron primarily deposits in the peritoneum.[8] The animals were kept under close observation and were killed when they showed persistent weight loss and/or distress. The experiments were terminated at 26.7 months of age. All the animals were autopsied. Samples were either immediately frozen and stored at $-80^{\circ}C$ until use, or subjected to routine histological analysis with buffered 10% formalin fixation and paraffin embedding. The animal experiment committees of the Graduate School of Medicine, Kyoto University and Nagoya University Graduate School of Medicine approved these animal experiments. All chemicals used were of analytical quality.

Rat Peritoneal Mesothelial Cells

Rat peritoneal mesothelial cells (RPMC) were cultured from the omentum of Wistar rats as previously described,[9] and grown in RPMI 1640 medium containing 10% fetal calf serum. A retroviral vector pCMSCVpuro-16E6E7 was constructed by recombining the segment of a donor vector containing full-length HPV16E6 and E7 (A kind gift from Dr Tohru Kiyono, National Cancer Center, Tokyo, Japan) into the destination vector by the Gateway System (Invitrogen Life Technologies, Carlsbad, CA, USA) as described previously.[10] RPMCs were infected at day 14 by the recombinant retrovirus expressing the 10A1 envelope[11] with 4 μg/ml polybrene, and were drug selected using 1 μg/ml puromycin.

Array-Based CGH Analysis

We performed array-based comparative genomic hybridization (aCGH) with a Rat Genome CGH Microarray 244A (G4435A; Agilent Technologies, Santa Clara, CA, USA), as described in the Agilent Oligonucleotide Array-based CGH for Genomic DNA Analysis Protocol ver. 5.0, and analyzed results with DNA Analytics Software (ver. 4.0). For each array, normal kidney was used as a reference and labeled with Cy-3. Samples of interest were labeled with Cy-5. Six cases of epithelioid mesotheliomas (EMs) and five cases of sarcomatoid mesotheliomas (SMs) were analyzed.

Fluorescent *In Situ* Hybridization

Appropriate bacterial artificial chromosome probes were selected from http://genome.ucsc.edu/ and purchased from http://bacpac.chori.org/. CH230-163D24 was used for *CDKN2A/2B*, and CH230-209G15 for *Erbb2*. Fluorescent probes were labeled by incorporating Green-dUTP (Vysis; Abbott Laboratories; Abott Park, IL, USA) into newly synthesized DNA by the Nick Translation Kit (Vysis). Fluorescent *in situ* hybridization (FISH) was performed using the probes, Paraffin Pretreatment Kit and LSI/WCP Hybridization Buffer (Vysis) according to the manufacturer's protocol. Briefly, paraffin sections were treated with protease, and after denaturation, the probes were hybridized to nuclear DNA, counterstained with DAPI, and visualized using a fluorescence microscope.

Expression Microarray Analysis

A total of 12 microarrays (Whole Rat Genome Microarray, G4131F; Agilent Technologies) were used for the screening purpose: four chips were used for tooth brush-scraped pleural and peritoneal mesothelial cells and soft tissue surrounding tunica vaginalis testis, six for EMs and two for SMs. Total RNA was isolated with an RNeasy Mini kit (QIAGEN GmbH, Hilden, Germany). Data analysis was performed using GeneSpring GX 10.02.2 software (Agilent Technologies).

Quantitative RT-PCR Analysis

Total RNA was extracted with RNeasy Mini (QIAGEN) and cDNA was synthesized using SuperScript III First-strand Synthesis System for RT-PCR (Invitrogen Life Technologies) with random primers. All of the primers used are summarized in the Supplementary Table 1.

Antibody

An anti-uromodulin rabbit polyclonal antibody was produced by a commercial supplier (Hokudo, Hokkaido, Japan). Briefly, a 15-mer polypeptide (NH_3-CKQDFNVTDVSLLEH-COOH) corresponding to the 320-334 cytoplasmic portion of rat UMOD protein (AAH81814) was synthesized and conjugated with keyhole limpet hemocyanin, which was used as an immunogen for JW rabbits. Five weeks after the second immunization, whole serum was harvested and purified using a SulfoLink Kit (Pierce, Rockford, IL, USA). Anti-S-100 polyclonal antibody (LSL-LB-9197) was from Cosmo Bio (Tokyo, Japan). Anti-desmin monoclonal antibody (clone D33) was from DAKO (Carpinteria, CA, USA). Anti-podoplanin polyclonal antibody (KS-17) was from Sigma (Saint Louis, MO, USA). Anti-multi-cytokeratin monoclonal antibody (RTU-AE1/AE3) was from Novocastra (Newcastle, UK). Anti-8-hydroxy-2′-deoxygunosine monoclonal antibody (clone N45.1)[12] was from Nikken Seil (Shizuoka, Japan). Anti-single stranded DNA antibody (no. 18731) was from IBL (Takasaki, Gunma, Japan).

Western Blot Analysis

This was performed using a standard procedure as previously described.[13,14]

Histology, Tissue Array, and Immunohistochemical Analysis

The specimens embedded in paraffin were cut at 3-μm thickness, stained with hematoxylin and eosin, or used for immunohistochemistry. Representative areas were chosen and cores of 3 mm diameter were punched out from the blocks with a precision instrument (Tissue Microprocessor; Azumaya, Tokyo, Japan). Those cores of 24 (6×4 array) in a group were embedded in a paraffin block. Immunohistochemistry was performed as previously described.[12] Antigen retrieval for single-stranded DNA was by incubation with proteinase K solution (Trevigen, Gaithersburg, MD, USA) at 37°C for 30 min. Negative controls are shown in the Supplementary Figure 1.

Detection of DNA-Strand Breaks

TUNEL (terminal deoxynucleotidyl transferase-mediated dUTP nick end labeling; TACS 2 TdT-Blue Label *In situ* Apoptosis Detection kit; Trevigen) method and immunohistochemical analysis for single-stranded DNA were used.

Statistical Analysis

Statistical analyses were performed with an unpaired *t*-test, which was modified for unequal variances when necessary. Kaplan–Meier analysis was also used. $P < 0.05$ was considered as statistically significant.

RESULTS

Two Distinct Pathologies were Observed in Ferric Saccharate-Induced Rat Peritoneal Mesothelioma

F1 hybrids between Fischer344 and Brown-Norway rat strains were used to allow allele-specific analyses when necessary. There was no significant difference in the survival between the control and iron-injected groups up to 20 months of age. Thereafter, animals in the iron-treatment group started to die from mesothelioma (Figure 1). Control animals generated no mesothelioma during the 26.7-month postnatal observation period. All observed tumors are summarized in Tables 1 and 2.

Two distinct pathologies were observed in the obtained mesotheliomas. The majority of tumors were observed in the vicinity of tunica vaginalis testis, and expanded to the upper peritoneal cavity in half of the cases (Figure 2). Most of the animals did not die from the disease during the observation period. When fine tumors were scattered throughout the whole peritoneum, we recognized these as malignant. Such tumors revealed papillary growth patterns and were always intensely positive for podoplanin and cytokeratin (Figure 2). These tumors were counterparts of human EM.

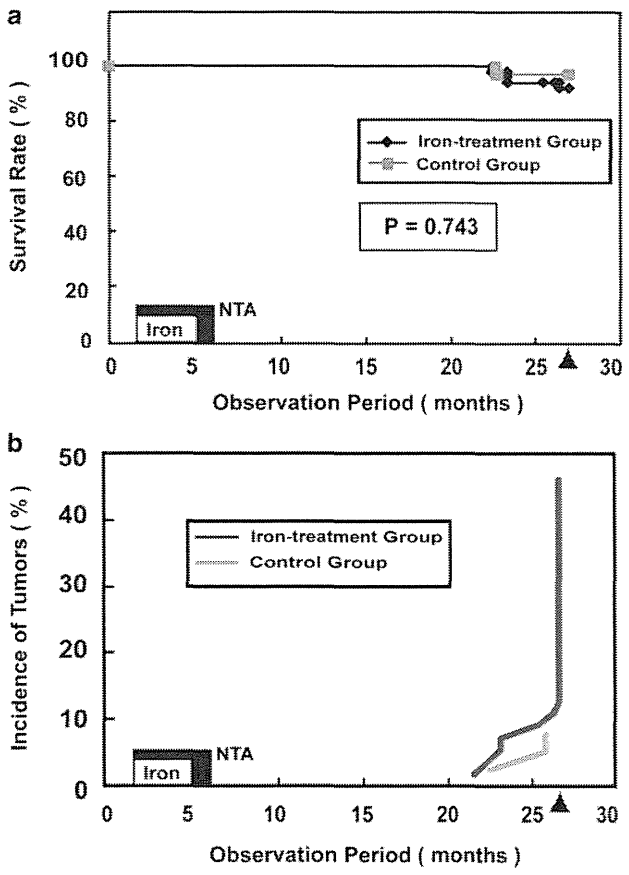

Figure 1 Survival rates (**a**) and incidence of tumors (**b**) in the iron-treatment group (iron saccharate followed by nitrilotriacetic acid) and the untreated control group. The arrow head shows the point of experiment termination (26.7 months after birth). NTA, nitrilotriacetic acid. Refer to Materials and methods section for details.

Table 1 Incidence of peritoneal mesothelioma by intraperitoneal injections of ferric saccharate and nitrilotriacetic acid

	Number of rats with mesothelioma	Number of rats with other tumors
Iron-treatment group		
Male ($N=24$)	16 (66.7%)	1 (4.2%)
Female ($N=30$)	1 (3.3%)	7 (23.3%)
Control group		
Male ($N=17$)	0 (0%)	2 (11.8%)
Female ($N=21$)	0 (0%)	1 (4.8%)

Numbers in parentheses show the animal numbers used in each group.

A second tumor type was found associated with intra-abdominal organs such as the stomach, spleen, and abdominal wall (Figure 2). These tumors showed strong invasive activity and sometimes presented as a mass involving several organs, omentum, and mesentery. Because of their invasive nature, these tumors were lethal primarily due to intestinal obstruction. Ascites was not observed. Histology showed high-grade spindle cell tumors, proliferating on the serosal surface of the organs. By immunohistochemical analysis, these tumors were cytokeratin-negative, desmin-negative but podoplanin-positive (weak to moderate). Immunohistochemistry for S-100 was sometimes weakly positive (Figure 2). Thus, these tumors represented counterparts of human SM. No transition from EM to SM was observed. Both tumor types, EM and SM, presented male preponderance (Table 1).

Array-Based CGH Analyses Classified Ferric Saccharate-Induced Rat Peritoneal Mesothelioma into Two Distinct Types

Six cases of EM and five cases of SM were analyzed by aCGH. Array-based CGH analysis clearly distinguished the two histological types. Although EMs showed numerous minor genomic amplifications and deletions, most of SMs showed a variety of chromosomal amplifications and deletions (Figure 3a). In particular, four out of the five cases of SM showed homozygous deletion of CDKN2A/2B, and in two cases amplification of ERBB2-containing region. The results obtained by aCGH were confirmed by FISH analysis (Figure 3b and c).

Expression Array Analysis Revealed Overexpression of Uromodulin in the Majority of Cases

Six cases of EM and two cases of SM were analyzed with expression microarray analyses (Table 2). The remaining cases of SM were not assayed by this technique because of poor-quality RNA, as the animals were found dead. Expression data for the 20 most strongly up- or downregulated genes are summarized in Tables 3 and 4 (Gene Expression Omnibus accession number GSE16138). We focused on uromodulin in this study as it is a major urinary protein,[15] and mesothelial cells and renal tubular cells are both of mesodermal origin. We confirmed the overexpression of this gene by RT-PCR analysis, western blot analysis, and immunohistochemistry (Figure 4). Brain, kidney, and testis in adult rats showed high expression of uromodulin.

Expression of Mesoderm-Specific Transcription Factors

Several mesoderm-specific early embryogenesis transcription factors were studied along with ectoderm- or endoderm-specific transcription factors. Out of the transcription factors examined, mesotheliomas showed activated DLX5,[16] ONECUT1 (HNF6),[17] and Pax6,[18] whereas the activation of HAND1,[19] ISL1,[20] and MEIS1[21] were not observed.

Oxidative Stress in Peritoneal Mesothelial Cells after Injection of Ferric Saccharate

Prominent iron deposition was found in the mesothelia and surrounding tissue including macrophages. Nuclear immunopositivity for 8-hydroxy-2′-deoxyguanosine (8-OHdG),[12] an oxidatively modified DNA product, was significantly increased in the mesothelia 4 weeks after repeated iron saccharate administration (Figure 5). At the same time, significant increase in DNA-strand breaks of the nuclear genomic DNA were observed in the mesothelia after iron treatment, based on TUNEL method (data not shown) and immunohistochemical analysis for single-stranded DNA (Figure 5).

DISCUSSION

In this study, we followed the established protocol to generate iron-induced peritoneal mesothelioma,[8,22] and analyzed the generated tumors using two different microarray techniques. An iron chelator, nitrilotriacetate, has been used in this fiber-unassociated mesothelioma model to mobilize the catalytic form of iron from deposits.[23,24] Our study revealed a number of important implications regarding mesothelioma, which is a serious social problem in many countries following asbestos exposure. From an epidemiological standpoint, asbestos fibers, in particular, crocidolite and amosite, are recognized to be more carcinogenic when containing high amounts of iron.[6] During the carcinogenenic experiments presented here, a relatively high amount of iron (a total of approximately 300 mg iron/kg body weight) was used. In contrast, only 15 mg iron/kg in the case of crocidolite or amosite is enough to produce high-grade mesothelioma in the majority of rats (Li J and Toyokuni S, unpublished data). Therefore, ferric saccharate is a much weaker carcinogen than crocidolite or amosite, considering the fact that most of the animals did not die from the disease up to 26.7 months. This suggests that the shape, size, and probably surface characteristics of the molecules are important contributing factors in mesothelial

Table 2 Pathological findings of all the induced tumors

Case	Original number	Cell type	Structure	Size of main tumor (mm)	Primary organ	Dissemination range (mm)
M1-male	1-1-male	EM	Papillary	<2 mm, multiple	Testis and peritoneum	120
M2-male	15-1-male	EM	Papillary	<2 mm, multiple	Testis	60
M3-male	15-2-male	EM	Papillary	<3 mm, multiple	Testis	30
M4-male	15-4-male	EM	Papillary	<3 mm, multiple	Testis	30
M5-male	15-5-male	EM	Papillary	<3 mm, multiple	Testis and peritoneum	120
M6-male	13-2-male	EM	Papillary	<2 mm, multiple	Testis and peritoneum	120
M7-male	10-4-male	SM	Solid	25	Stomach and spleen	NA
M8-female	12-4-female	SM	Solid	30	Abdominal wall	NA
M9-male	11-2-male	SM	Solid	50	Stomach	NA
M10-male	13-1-male	SM	Solid	50	Abdominal wall	NA
M11-male	13-2-2-male	SM	Solid	100	Stomach and omentum	150
M12-male	8-2-male	EM	Papillary	<1 mm, multiple	Testis	20
M13-male	8-3-male	EM	Papillary	<1 mm, multiple	Testis	30
M14-male	10-2-male	EM	Papillary	<1 mm, multiple	Testis	<5 mm
M15-male	10-3-male	EM	Papillary	<1 mm, multiple	Testis	<5 mm
M16-male	11-1-2-male	EM	Papillary	<1 mm, multiple	Testis	<5 mm
M17-male	13-3-male	EM	Papillary	<1 mm, multiple	Testis	10
T1-female	M-2-1	Fibroadenoma	Solid	30	Mammary gland	NA
T2-female	M-2-4	Fibroadenoma	Solid	50	Mammary gland	NA
T3-female	M-4-1	Fibroadenoma	Solid	40	Mammary gland	NA
T4-female	M-4-3	Fibroadenoma	Solid	80	Mammary gland	NA
T5-female	M-6-2	Fibroadenoma	Solid	100	Mammary gland	NA
T6-female	M-7-1	Fibroadenoma	Solid	40	Mammary gland	NA
T7-female	M-14-2	Mature cystic teratoma	Solid	50	Ovary	NA
T8-male	O-10-1	Leydig cell tumor	Papillary	6	Testis	NA
C1-male	O-17-4	Hepatocellular carcinoma	Solid	50	Liver	NA
C2-male	O-21-3	Fibrolipoma	Solid	80	Soft tissue	NA
C3-female	M-22-4	Fibroadenoma	Solid	10	Mammary gland	NA

EM, epithelioid mesothelioma; SM, sarcomatoid mesothelioma; NA, not applied.

M1-11 and M1-8 were used for array-based comparative hybridization analyses and expression microarray analyses, respectively.

carcinogenesis. Here, paradoxically the weaker carcinogenesis model did present several novel viewpoints.

First, these experiments revealed a clear preference for tumorigenesis in males. This observation is consistent with the accumulated human epidemiological data.[25] However, in the case of humans, differences in frequency and doses of asbestos exposure between males and females must be considered. Our results indicate that sex hormone and/or anatomical differences such as the presence of tunica vaginalis are also contributing factors in the generation of mesothelioma.

We classified mesotheliomas into two types: low-grade and high-grade. Low-grade tumors were of the epithelioid type,[26] originating from the vicinity of tunica vaginalis testis. Some of these tumors disseminated to the whole abdominal cavity. High-grade tumors were of the sarcomatoid type, originating in the upper abdominal cavity. Fischer-344 strain rats are known to generate testicular mesothelioma albeit at a low incidence (0–1.3%).[27,28] To control this situation, we have used F1 hybrid rats crossed between Fischer-344 and Brown-Norway strains, and the hybrid animals in these experiments presented no mesothelioma in the untreated control group. Therefore, we believe that our data was not affected significantly by the background of genetic susceptibility to mesothelioma.

We confirmed the histological diagnoses by immunohistochemistry in a similar manner as applied to human cases

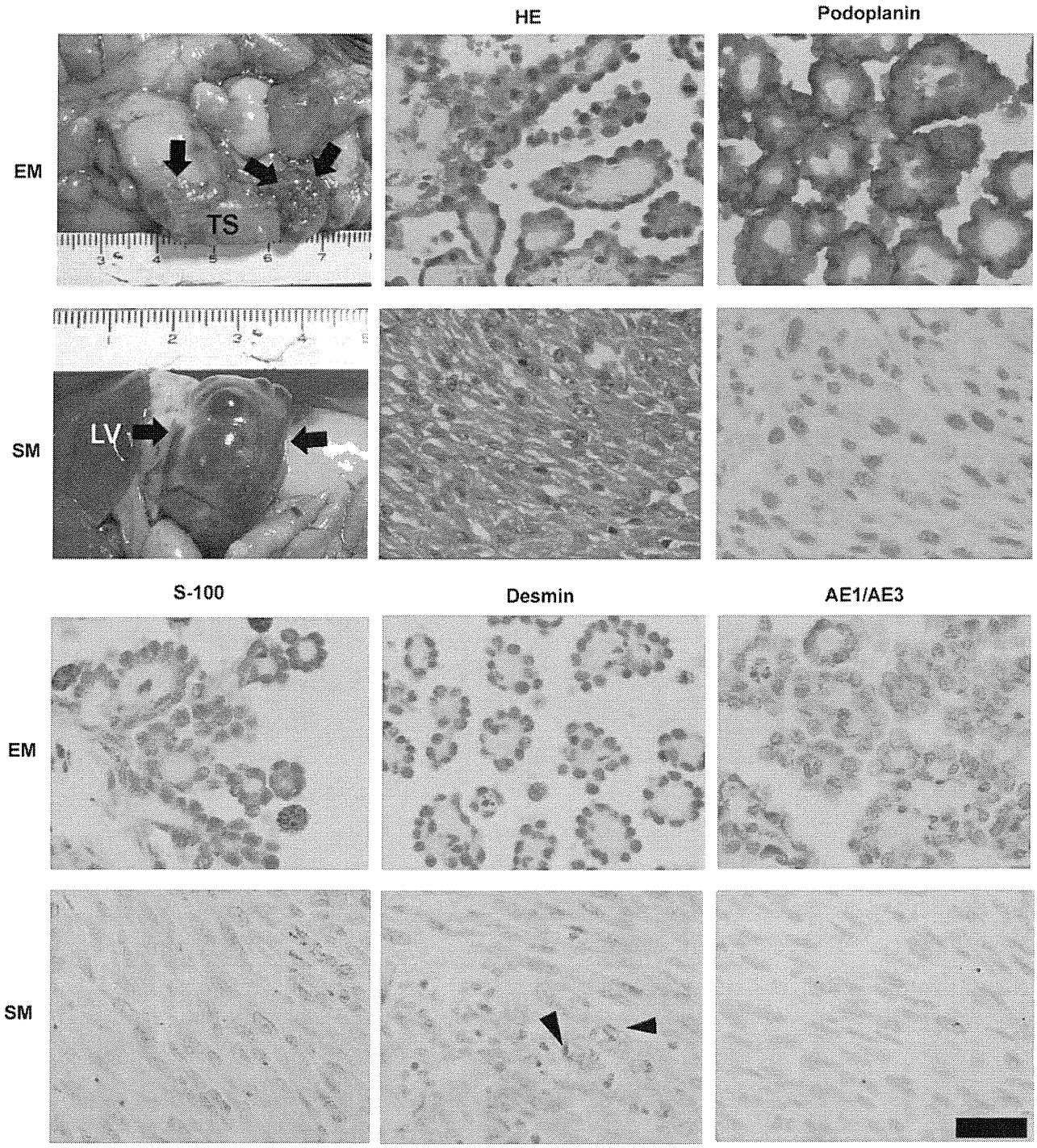

Figure 2 Two distinct types of mesothelioma induced by iron saccharate and nitrilotriacetic acid. EM, epithelioid-type. SM, sarcomatoid-type. Podoplanin was immunostained with red color, whereas S-100, desmin, and pancytokeratin are shown in brown. The arrows indicate mesothelioma. TS, testis. LV, liver. Arrowheads, smooth muscle in vessels (bar = 100 μm).

of mesothelial tumors.[26] Epithelioid types were strongly positive for podoplanin, and sarcomatoid types were negative for desmin (myogenic marker). Unfortunately, many antibodies are not available for rats. Sarcomatoid tumor types showed weak-to-moderate positivity for podoplanin and no positivity for pan-keratin in our study. Some of the cases showed weak positivity for S-100. Such cases are also described in human mesotheliomas.[26] Of note was the fact that these two types of tumors were clearly different in their aCGH profiles. Importantly, most of the sarcomatoid type tumors examined showed homozygous deletion of CDKN2A/2B ($p16^{INK4A}$/$p15^{INK4B}$) with two cases of *ERBB2* amplification.

ERBB2 is a receptor tyrosine kinase for epidermal growth factor.[29,30] Activation of *ERBB2* is reported in human mesothelioma cell lines.[31] Our present study demonstrated that oxidative stress is a cause of *ERBB2* amplification. Inactivation of *CDKN2A/2B* is the second most common genetic event in human cancers next to *p53* tumor suppressor gene alterations.[32] There are three different mechanisms of inactivation: (i) homozygous deletion, (ii) inactivating mutation with loss of heterozygosity, and (iii) methylation of the CpG island promoter region. It is probably not a coincidence that *CDKN2A/2B* is a major tumor suppressor gene target in ferric nitrilotriacetate (Fe-NTA)-induced rat renal carcinogenesis model,[33] in which a major mode of inactivation is also homozygous deletion.[34,35] In the renal carcinogenesis model, an iron-catalyzed Fenton reaction is repeatedly induced in the target renal proximal tubular cells early in carcinogenesis[36–38] These data strongly suggest that iron-mediated oxidative DNA damage is a major cause of the homozygous deletion of *CDKN2A/2B*. Interestingly, potassium bromate shares with iron compounds the ability to cause not only mesothlioma[28] but also renal cell carcinoma [39] presumably by oxidative stress.[40]

For the homozygous deletion to occur, DNA double-strand breaks (DSBs) should be present, either as DNA damage or endogenous mechanisms. The presence of DSBs in the genomic DNA during replication is expected to result in homozygous deletion. So far, it is established that γ-radiation, ultraviolet radiation, and transition metals are causative agents of DNA DSBs.[41,42] Furthermore, various repair processes of DNA base modifications.[43] or hypermutation with increased activity of activation-induced deaminase can be endogenous causes of DSBs.[44–46] In many cases of human leukemias, which can be induced by γ-radiation,[47] translocations and deletions are frequently observed.[48,49] However, as far as we know in animal carcinogenesis models, massive chromosomal alterations as seen in the high-grade mesothelioma and Fe-NTA-induced renal cell carcinoma[14] have not been reported, except for genetically engineered mice leading to malignant lymphoma.[50] These results emphasize the importance of iron-mediated oxidative stress in carcinogenesis. Indeed, at the evaluation of the peritoneum 4 weeks after the start of the experiment, iron deposition was clear in the mesothelial cells with evidence of oxidative stress and DNA-strand breaks. Previously, we demonstrated *in vitro* that 8-OHdG formation and single/double-strand breaks in DNA are proportional.[51] 8-OHdG is produced either by ·OH, $^1O_2$, or photodynamic action. Iron is closely associated with ·OH generation as a catalyst in Fenton reaction,[52] and provides a mutation-prone environment that stochastically culminates in tumorigenesis. Thus, the iron-induced animal carcinogenesis presents an ideal model how *CDKN2A/2B* is selected as a target of homozygous deletion in a situation where DNA DSBs and *CDKN2A/2B* are associated in terms of a senescence-like condition.[53] We are currently working on how specific amplification and deletion in the genome are generated by the use of a methodology called oxygenomics.[54]

Next, we would like to discuss how the two different types of mesothelioma are generated. Interestingly, EMs were produced at the lowest point of the body in male animals. It is possible that iron deposition is more prominent around tunica vaginalis testis in males. In contrast, special unidentified mesothelial cells prone to transformation may be present in this anatomical location. In human pleural mesotheliomas, homozygous deletion of *CDKN2A/2B* is present in a majority of cases (69% in EMs and 100% in SMs).[55] This implies that the EMs in our study with no prominent chromosomal instability are at early stages and that deletion of *CDKN2A/2B* is not always necessary for the induction of EMs. On the contrary, all the SMs occurred at the upper abdominal area, concomitant with homozygous deletion of *CDKN2A/2B* in 80% of the cases. Although iron overload appears important to generate the homozygous deletion of *CDKN2A/2B*, we suspect that increased oxygen tension by repeated intraperitoneal injections at the upper abdominal area might have assisted this genomic alteration as oxygen tension of the peritoneal cavity is maintained much lower than the atmosphere.[56] Another contributing factor could be abundant adipocytes in the omentum and mesentery. It is possible that secretion of a variety of cytokines by adipocytes and inflammatory macrophages may have modulated carcinogenesis after iron overload.[57] It also remains elusive whether mesothelioma truly originates from surface mesothelial cells, as mesothelial cells and lymphatic cells are seamlessly connected in the parietal pleura.[58]

In expression microarrays, it is important to choose appropriate control samples. In the case of mesothelioma, this is not trivial. We have tried two different samples, namely, brush-scraped surface cells from the pleural and abdominal cavity and soft tissue surrounding the tunica vaginalis testis, and the average was used. Following expression profiling, we focused primarily on uromodulin and transcription factors associated with early mesodermal differentiation. Uromodulin showed the most significant change, especially in EMs. Uromodulin has been recognized as the most

Figure 3 Array-based comparative genome hybridization analysis of mesotheliomas. (**a**) Whole genome data. EM, epithelioid-type. SM, sarcomatoid-type. Numbers denote the rat chromosome number. Sarcomatoid-type tumors revealed more extensive chromosomal alterations than epithelioid-type tumors. (**b**) Data from the long-arm of chromosome 5 in sarcomatoid mesothelioma. Common homozygous deletion of *p16* (*CDKN2A*) and *p15* (*CDKN2B*) is observed. Inset shows the magnification of *CDKN2A/2B* area (longitudinal line shows the exact gene location). Representative data from FISH analysis are shown (orange signals under DAPI nuclear counterstaining; left, splenic lymphocytes; right, mesothelioma). (**c**) Data from the long-arm of chromosome 10 in sarcomatoid mesothelioma. Common amplification of *ERBB2* is observed. Inset shows the magnification of *ERBB2* area (longitudinal line shows the exact gene location). Representative data from FISH analysis are shown (green signals under DAPI nuclear counterstaining; two mesotheliomas with or without *ERBB2* amplification).

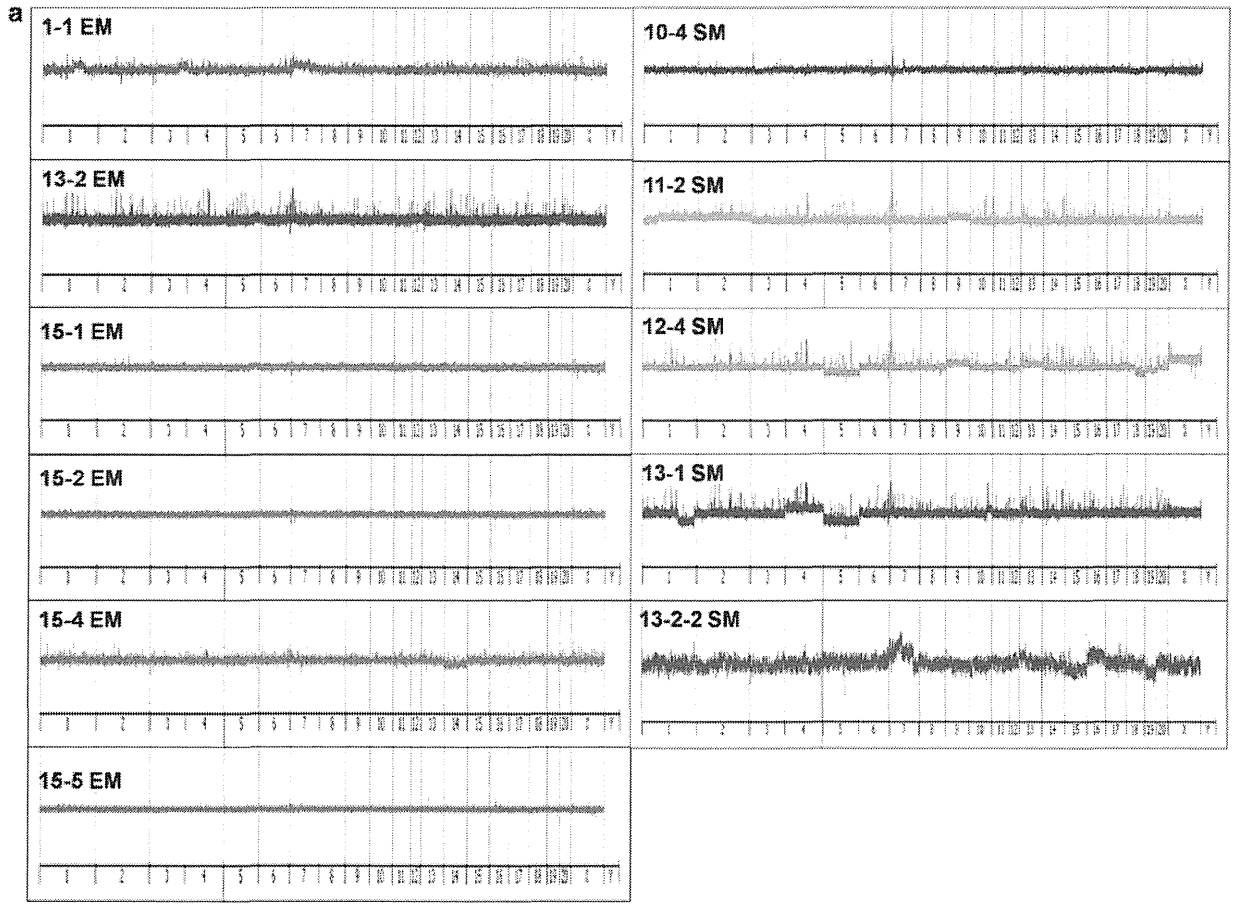
a
1-1 EM
10-4 SM
13-2 EM
11-2 SM
15-1 EM
12-4 SM
15-2 EM
13-1 SM
15-4 EM
13-2-2 SM
15-5 EM

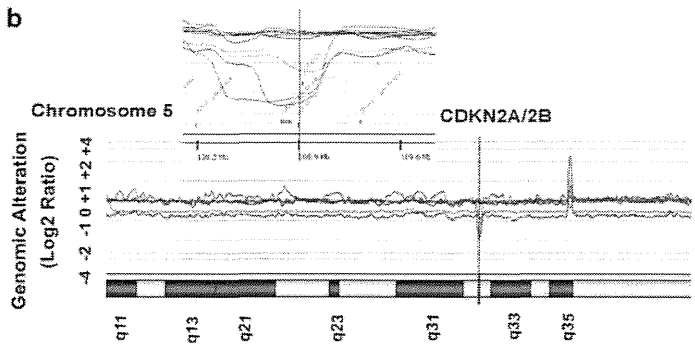
b
Chromosome 5
CDKN2A/2B
Genomic Alteration (Log2 Ratio)
-4 -2 -1 0 +1 +2 +4
q11
q13
q21
q23
q31
q33
q35

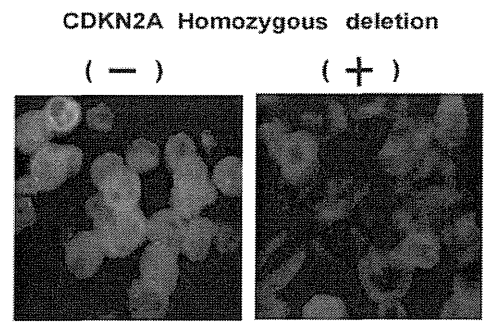
CDKN2A Homozygous deletion
(—)
(+)

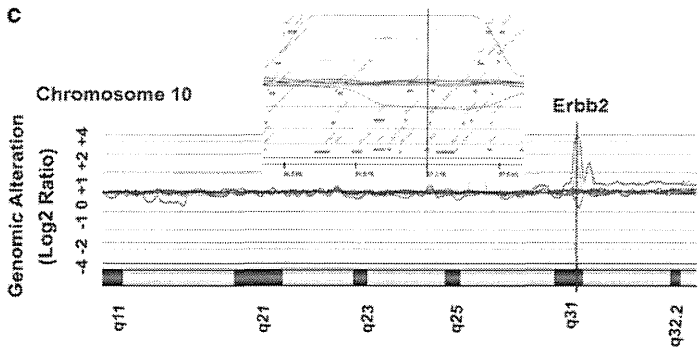
c
Chromosome 10
Erbb2
Genomic Alteration (Log2 Ratio)
-4 -2 -1 0 +1 +2 +4
q11
q21
q23
q25
q31
q32.2

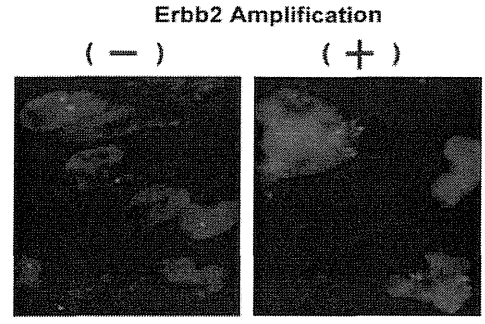
Erbb2 Amplification
(—)
(+)

Table 3 Top 20 Upregulated genes in iron-induced mesothelioma

GenBank no.	Gene description	Fold change (log2)
Genes upregulated	Epithelioid mesothelioma	
NM_001017496	Similar to small inducible cytokine B13 precursor (CXCL13)	9.218209417
NM_001008831	RT1 class II, locus Ba (RT1-Ba)	8.71250575
NM_017082	Uromodulin (Umod)	7.9219705
NM_022175	Placentae and embryos oncofetal gene (Pem)	7.658948067
U15550	Tenascin-C	7.634158617
NM_012881	Secreted phosphoprotein 1 (Spp1)	7.575371133
NM_024142	Matrix extracellular phosphoglycoprotein with ASARM motif (bone) (Mepe)	7.260534987
NM_001008560	Protease, serine, 35 (Prss35)	7.201287705
NM_013028	Short stature homeobox 2 (Shox2),	7.152587133
NM_017216	Solute carrier family 3, member 1 (Slc3a1)	7.004159133
NM_031757	Matrix metallopeptidase 24 (Mmp24)	6.9717793
NM_030837	Kidney-specific organic anion transporter (Slc21a4)	6.9573312
NM_001024893	Similar to melanoma antigen family A, 5 (MGC114427)	6.673916917
NM_031044	Histamine N-methyltransferase (Hnmt)	6.611724693
NM_017210	Deiodinase, iodothyronine, type III (Dio3)	6.5584509
ENSRNOT00000020919	Glia-derived nexin precursor (GDN) (Protease nexin I) (PN-1)	6.543974733
NM_019134	Solute carrier family 12, member 1 (Slc12a1)	6.519795817
NM_012995	Oncomodulin (Ocm)	6.427419253
NM_175760	Cytochrome P450, family 4, subfamily a, polypeptide 14 (Cyp4a14)	6.383245517
NM_022590	Solute carrier family 5 (sodium/glucose cotransporter), member 2 (Slc5a2)	6.297669483
Genes upregulated	*Sarcomatoid mesothelioma*	
NM_001008560	Protease, serine, 35 (Prss35)	8.482390353
ENSRNOT00000003452	Tenascin N (predicted) (Tnn_predicted)	8.014980133
NM_001008831	RT1 class II, locus Ba (RT1-Ba)	7.632204375
NM_013028	Short stature homeobox 2 (Shox2)	7.028548317
ENSRNOT00000056534	Fragile X mental retardation 1 neighbor (Fmr1nb_predicted)	7.009716683
NM_133523	Matrix metallopeptidase 3 (Mmp3)	6.860669808
ENSRNOT00000031175	Cellular retinoic acid-binding protein 1(CRABP-I)	6.7431448
U15550	Tenascin-C	6.739385108
NM_012881	Secreted phosphoprotein 1 (Spp1)	6.479985417
NM_019282	Gremlin 1 homolog, cysteine knot superfamily (Xenopus laevis) (Grem1)	6.262645658
NM_172333	Collagen triple helix repeat containing 1 (Cthrc1)	6.101469273
ENSRNOT00000020919	Glia-derived nexin precursor (GDN) (Protease nexin I) (PN-1)	5.882276717
NM_001006993	Sarcoglycan, gamma (dystrophin-associated glycoprotein) (Sgcg)	5.860486633
ENSRNOT00000011507	Collagenase 3 precursor (EC 3.4.24.-) (Matrix metalloproteinase-13) (MMP-13)	5.846046783
NM_053881	Protein tyrosine phosphatase, receptor type, N (Ptprn)	5.760772425
NM_021666	Triadin (Trdn)	5.510140083
NM_012980	Matrix metallopeptidase 11 (Mmp11)	5.505010658
NM_013046	Thyrotropin releasing hormone (Trh)	5.49094599
NM_001025155	Leucine-rich repeat containing 17 (Lrrc17)	5.43975145
NM_013153	Hyaluronan synthase 2 (Has2)	5.407057475

Table 4 Top 20 Downregulated genes in iron-induced mesothelioma

GenBank no.	Gene description	Fold change (log2)
Genes downregulated	Epithelioid mesothelioma	
ENSRNOT00000006885	PREDICTED: similar to cystatin E2	−8.73490455
NM_138842	Surfactant-associated protein B (Sftpb)	−8.402350217
NM_138854	Solute carrier family 38, member 5 (Slc38a5)	−7.91033265
NM_053983	CD52 antigen (Cd52)	−7.259246867
XM_574039	PREDICTED: glutathione peroxidase 5 (Gpx5)	−7.182397383
NM_153301	Arachidonate 15-lipoxygenase, second type (Alox15b)	−7.109294617
NM_139085	Cystatin 11 (Cst11)	−7.021647783
NM_144744	Adiponectin, C1Q and collagen domain containing (Adipoq)	−6.90978975
NM_001012056	Carboxylesterase 615 (LOC307660)	−6.658661367
NM_001001519	Lipocalin 6 (Lcn6)	−6.620507583
NM_001009524	Beta-galactosidase-like protein (Bin2a)	−6.5667172
NM_139339	Tramdorin 1 (Slc36a2)	−6.48272195
ENSRNOT00000044284	PREDICTED: lipocalin 9 (predicted) (Lcn9_predicted)	−6.467987617
NM_019258	Cystatin 8 (cystatin-related epididymal spermatogenic) (Cst8)	−6.3628091
NM_017342	Surfactant-associated protein C (Sftpc)	−6.166993217
NM_001008561	Ribonuclease, RNase A family, 9 (non-active) (Rnase9)	−5.987007817
NM_134326	Albumin (Alb)	−5.957892917
NM_053730	Stromal antigen 3 (Stag3)	−5.949726633
NM_001001934	Lymphocyte antigen 6 complex, locus G5B (Ly6g5b)	−5.9309187
NM_153734	Cystatin TE-1 (LOC266776)	−5.847135583
Genes downregulated	Sarcomatoid mesothelioma	
NM_138842	Surfactant-associated protein B (Sftpb)	−9.550074108
NM_053983	CD52 antigen (Cd52)	−8.859255933
ENSRNOT00000006885	PREDICTED: similar to cystatin E2	−8.451462275
XM_574039	PREDICTED: glutathione peroxidase 5 (Gpx5)	−8.209176692
NM_138854	Solute carrier family 38, member 5 (Slc38a5)	−7.371380075
NM_139085	Cystatin 11 (Cst11)	−7.356058742
NM_001001519	Lipocalin 6 (Lcn6)	−6.846685092
NM_153301	Arachidonate 15-lipoxygenase, second type (Alox15b)	−6.697708308
NM_001009524	Beta-galactosidase-like protein (Bin2a)	−6.5989881
NM_001009540	Tumor-associated calcium signal transducer 2 (Tacstd2)	−6.56866565
NM_001008561	Ribonuclease, RNase A family, 9 (non-active) (Rnase9)	−6.462160908
NM_001012056	Carboxylesterase 615 (LOC307660)	−6.120110183
NM_001004236	Tetraspanin 1 (Tspan1)	−6.071135933
NM_019258	Cystatin 8 (cystatin-related epididymal spermatogenic) (Cst8)	−6.01918205
NM_147213	Alpha-2u globulin PGCL5 (LOC259245)	−6.012992958
NM_139339	Tramdorin 1 (Slc36a2)	−5.990390975
ENSRNOT00000044284	PREDICTED: lipocalin 9 (predicted) (Lcn9_predicted)	−5.982269108
NM_001006990	Cell adhesion molecule JCAM (LOC304000)	−5.772606325
NM_001001934	Lymphocyte antigen 6 complex, locus G5B (Ly6g5b)	−5.756341
NM_053730	Stromal antigen 3 (Stag3)	−5.744070067

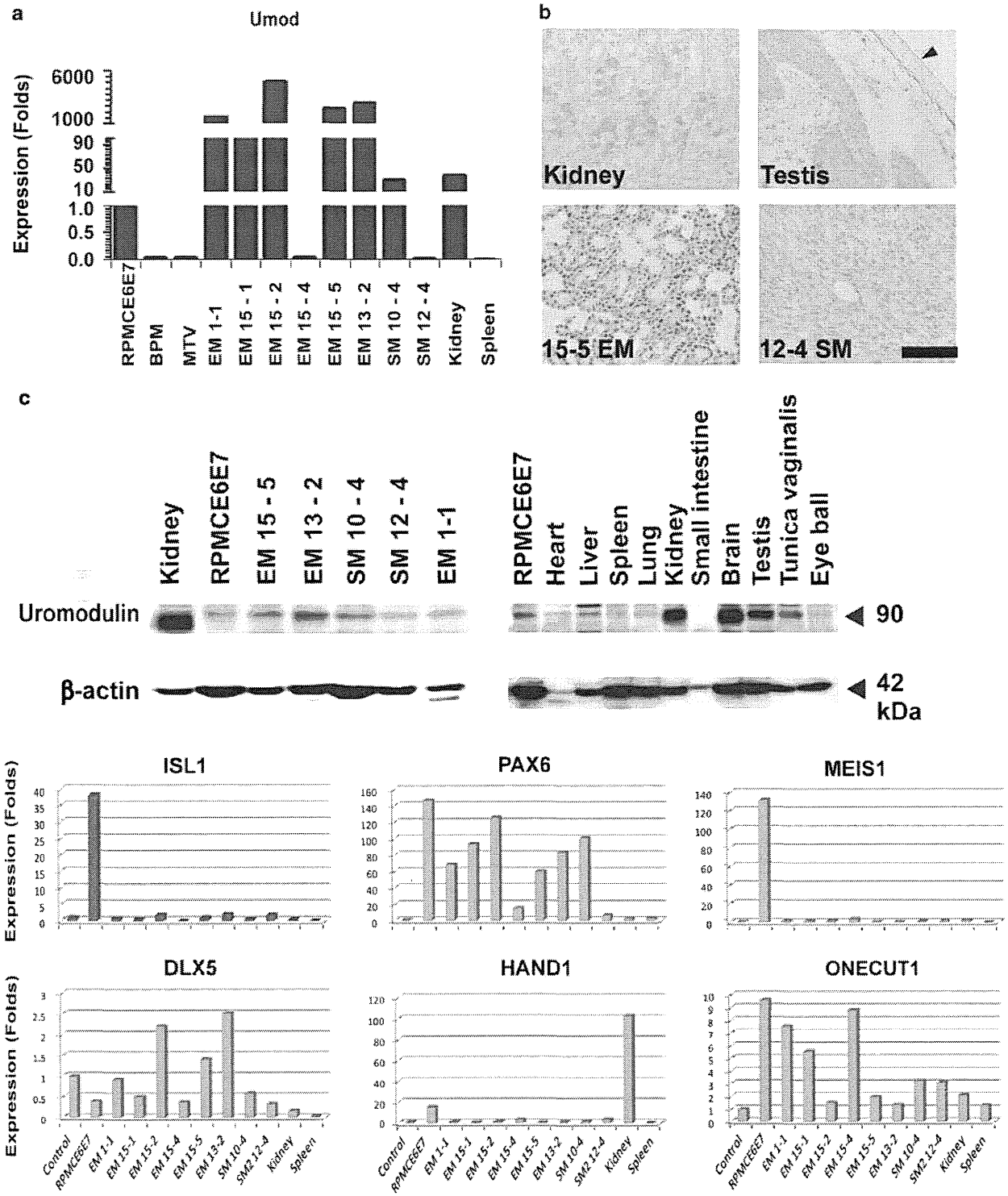

Figure 4 Expression analysis of uromodulin and mesoderm-associated transcription factors. (**a**) Levels of uromodulin message in iron-induced mesothelioma. RPMCE6E7, rat peritoneal mesothelial cells expressing E6 and E7; BPM, brushed pleural/peritoneal cells (rat); MTV, mesothelial cells surrounding tunica vaginalis testis. (**b**) Immunohistochemical analysis of uromodulin. Renal tubular cells in the ascending loop of Henle and seminiferous tubules in testis are well immunostained (Control organs are from an 8-week-old male Wistar rat). Arrowhead shows immunostaining-negative mesothelium (bar = 100 μm in kidney and testis; 200 μm in mesothelioma). (**c**) Western blot analysis of uromodulin. (**d**) Expression analysis of various embryonal transcriptional factors. PAX6 and MEIS1, ectodermal; DLX5, HAND1 and ONECUT1, mesodermal; ISL1, ectodermal/endodermal.

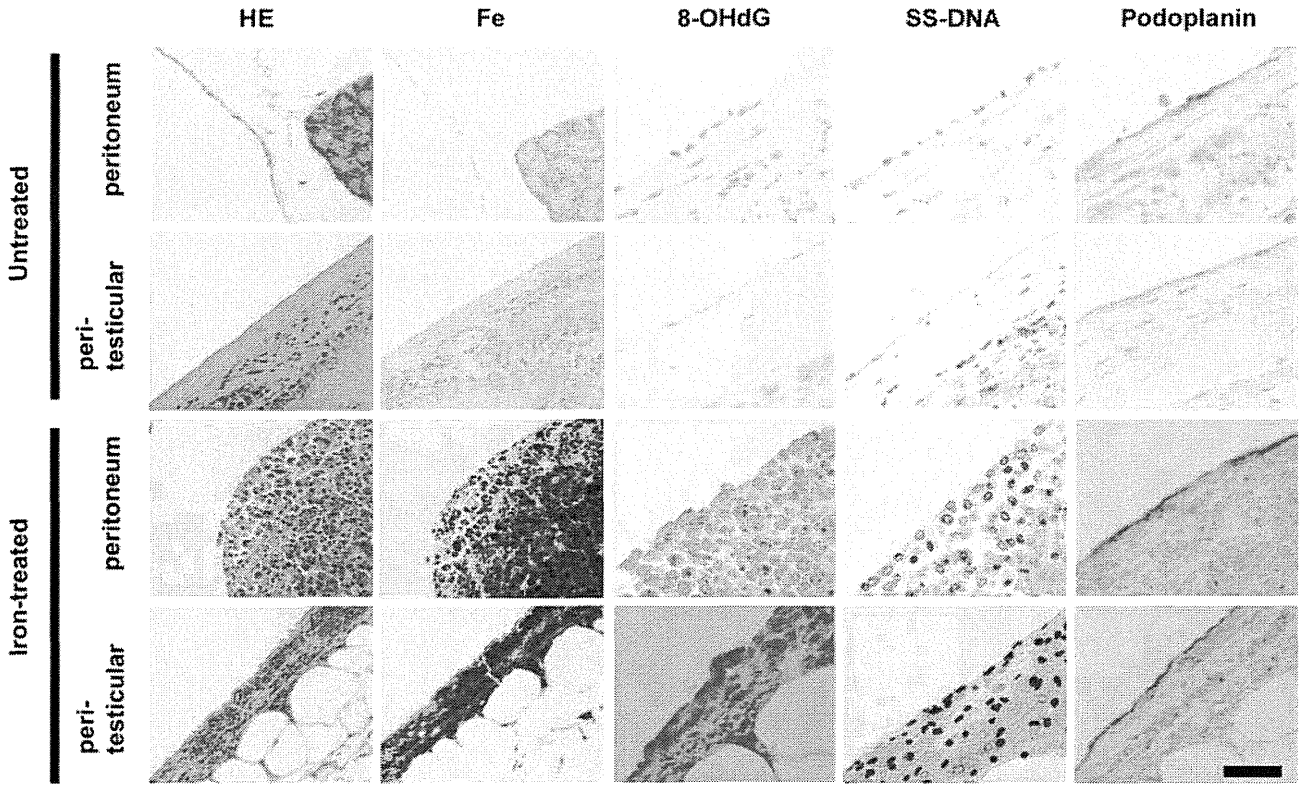

Figure 5 Analysis of oxidative stress in mesodermal cells 4 weeks after repeated iron saccharate administration. After iron-treatment, hemosiderin deposition in mesothelia and macrophages is prominent in subperitoneal areas, as demonstrated by Perls' iron staining (shown in green color). Nuclear 8-hydroxy-2′deoxyguanosine (8-OHdG) (shown in red color) and DNA single-strand breaks (shown in blue color) are increased in mesothelia after iron-treatment with immunohistochemical analyses. Surface swollen cells show podoplanin-positivity, demonstrating that they are mesothelial cells. SS-DNA, single-stranded DNA (bar = 100 μm in the right three columns; 200 μm in the left two columns).

abundant urinary protein,[15] and is immunosuppressive through interaction with interleukin 1α [59] and tumor necrosis factor by its lectin-like activity.[60] In this way, uromodulin may protect mesothelioma cells from the attack of immune cells. Regarding the discrepancy between mRNA and protein levels in the kidney and mesothelia (Figure 4a and c), we are currently studying it at the three different levels: microRNA, protein stability, and secretion.

Interestingly, we found that iron saccharate-induced mesotheliomas were driven by mesoderm-specific transcription factors, DLX5[16] and ONECUT1 (HNF6),[17] but not HAND1.[19] It is to be noted that an ectoderm-associated transcription factor, PAX6, was also activated. Thus, these molecules can be novel markers for early diagnosis and therapeutic targets if the situation is the same for human mesothelioma. Serum osteopontin (also as secreted phosphoprotein 1) levels have been proposed as a marker of mesothelioma and asbestos exposure[61–63] We could confirm this in our expression microarray profiles. Other up- or downregulated genes listed in the Tables 3 and 4 are under investigation for their roles in carcinogenesis.

In conclusion, we found two distinct pathologic types in the iron saccharate-induced mesothelioma rat model. In high-grade tumors, homozygous deletion of *CDKN2A/2B* was observed except only one case. Thus, our data strongly support that iron overload induces homozygous deletion of *CDKN2A/2B*. At the same time, iron overload is a major risk factor for the generation of mesothelioma, and any condition to induce peritoneal iron overload may eventually increase the risk for mesothelioma. Several genetically engineered mesothelioma models demonstrated the essential role of *NF2*, *CDKN2A/ARF*, and *P53* in mesothelial carcinogenesis.[64,65] However, it remains elusive how oxidative DNA damage catalyzed by iron leads to specific homozygous deletion of *CDKN2A/2B*. In this sense, this model is appropriate for the further study of mesothelial carcinogenesis and its preventive intervention.

Supplementary Information accompanies the paper on the Laboratory Investigation website (http://www.laboratoryinvestigation.org)

ACKNOWLEDGEMENT

This work was supported in part by a MEXT grant (Special Coordination Funds for Promoting Science and Technology), a Grant-in-Aid for Cancer Research from the Ministry of Health, Labour and Welfare of Japan, and a Grant-in-Aid from the Ministry of Education, Culture, Sports, Science and Technology of Japan.

DISCLOSURE/CONFLICT OF INTEREST

The authors declare no conflict of interest.

1. Toyokuni S. Iron-induced carcinogenesis: the role of redox regulation. Free Radic Biol Med 1996;20:553–566.
2. Toyokuni S. Role of iron in carcinogenesis: cancer as a ferrotoxic disease. Cancer Sci 2009;100:9–16.
3. Roggli VL, Oury TD, Sporn TA. Pathology of asbestos-associated diseases. Springer Verlag: New York, 2004.
4. Toyokuni S. Mechanisms of asbestos-induced carcinogenesis. Nagoya J Med Sci 2009;71:1–10.
5. Kamp DW, Graceffa P, Pryor WA, *et al.* The role of free radicals in asbestos-induced diseases. Free Radic Biol Med 1992;12:293–315.
6. McDonald A, McDonald J, Pooley F. Mineral fibre content of lung in mesothelial tumours in North America. Ann Occup Hyg 1982;26:417–422.
7. Wang N, Jaurand M, Magne L, *et al.* The interactions between asbestos fibers and metaphase chromosomes of rat pleural mesothelial cells in culture. A scanning and transmission electron microscopic study. Am J Pathol 1987;126:343–349.
8. Okada S, Hamazaki S, Toyokuni S, *et al.* Induction of mesothelioma by intraperitoneal injections of ferric saccharate in male Wistar rats. Br J Cancer 1989;60:708–711.
9. Oravecz T, Pall M, Roderiquez G, *et al.* Regulation of the receptor specificity and function of the chemokine RANTES (regulated on activation, normal T cell expressed and secreted) by dipeptidyl peptidase IV (CD26)-mediated cleavage. J Exp Med 1997;186: 1865–1872.
10. Yamashita Y, Tsurumi T, Mori N, *et al.* Immortalization of Epstein-Barr virus-negative human B lymphocytes with minimal chromosomal instability. Pathol Int 2006;56:659–667.
11. Naviaux R, Costanzi E, Haas M, *et al.* The pCL vector system: rapid production of helper-free, high-titer, recombinant retroviruses. J Virol 1996;70:5701–5705.
12. Toyokuni S, Tanaka T, Hattori Y, *et al.* Quantitative immunohistochemical determination of 8-hydroxy-2′-deoxyguanosine by a monoclonal antibody N45.1: its application to ferric nitrilotriacetate-induced renal carcinogenesis model. Lab Invest 1997;76:365–374.
13. Toyokuni S, Kawaguchi W, Akatsuka S, *et al.* Intermittent microwave irradiation facilitates antigen-antibody reaction in Western blot analysis. Pathol Int 2003;53:259–261.
14. Liu Y-T, Shang D-G, Akatsuka S, *et al.* Chronic oxidative stress causes amplification and overexpresson of ptprz1 protein tyrosine phosphatase to activate β-catenin pathway. Am J Pathol 2007;171:1978–1988.
15. Prasadan K, Bates J, Badgett A, *et al.* Nucleotide sequence and peptide motifs of mouse uromodulin (Tamm-Horsfall protein)—the most abundant protein in mammalian urine. Biochim Biophys Acta 1995;1260:328–332.
16. Miyama K, Yamada G, Yamamoto T, *et al.* A BMP-inducible gene, dlx5, regulates osteoblast differentiation and mesoderm induction. Dev Biol 1999;208:123–133.
17. Khoo M, McQuade L, Smith M, *et al.* Growth and differentiation of embryoid bodies derived from human embryonic stem cells: effect of glucose and basic fibroblast growth factor. Biol Reprod 2005;73:1147–1156.
18. Li H, Yang J, Jacobson R, *et al.* Pax-6 is first expressed in a region of ectoderm anterior to the early neural plate: implications for stepwise determination of the lens. Dev Biol 1994;162:181–194.
19. Firulli A, McFadden D, Lin Q, *et al.* Heart and extra-embryonic mesodermal defects in mouse embryos lacking the bHLH transcription factor Hand1. Nat Genet 1998;18:266–270.
20. Lin L, Bu L, Cai C, *et al.* Isl1 is upstream of sonic hedgehog in a pathway required for cardiac morphogenesis. Dev Biol 2006;295: 756–763.
21. Hisa T, Spence S, Rachel R, *et al.* Hematopoietic, angiogenic and eye defects in Meis1 mutant animals. EMBO J 2004;23:450–459.
22. Maronpot R, Zeiger E, McConnell E, *et al.* Induction of tunica vaginalis mesotheliomas in rats by xenobiotics. Crit Rev Toxicol 2009;39:512–537.
23. Okada S, Hamazaki S, Ebina Y, *et al.* Nephrotoxicity and its prevention by vitamin E on ferric nitrilotriacetate-promoted lipid peroxidation. Biochim Biophys Acta 1987;922:28–33.
24. Toyokuni S, Sagripanti J-L. DNA single- and double-strand breaks produced by ferric nitrilotriacetate in relation to renal tubular carcinogenesis. Carcinogenesis 1993;14:223–227.
25. Pass HI, Vogelzang NJ, Carbone M. Malignant mesothelioma: Advances in pathogenesis, diagnosis, and translational therapies. Springer Science+Business Media Inc: New York, NY, 2005.
26. Churg A, Cagle PT, Roggli VL. Tumors of the serosal membranes. ARP Press: Silver Spring, Maryland, 2006.
27. Damjanov I, Friedman M. Mesotheliomas of tunica vaginalis testis of Fischer 344 (F344) rats treated with acrylamide: a light and electron microscopy study. In Vivo 1998;12:495–502.
28. Wolf D, Crosby L, George M, *et al.* Time- and dose-dependent development of potassium bromate-induced tumors in male Fischer 344 rats. Toxicol Pathol 1998;26:724–729.
29. Yamamoto T, Ikawa S, Akiyama T, *et al.* Similarity of protein encoded by the human *c-erb-B-2* gene to epidermal growth factor receptor. Nature 1986;319:230–234.
30. Borg A, Baldetorp B, Ferno M, *et al. ERBB2* amplification in breast cancer with a high rate of proliferation. Oncogene 1991;6: 137–143.
31. Kawaguchi K, Murakami H, Taniguchi T, *et al.* Combined inhibition of MET and EGFR suppresses proliferation of malignant mesothelioma cells. Carcinogenesis 2009;30:1097–1105.
32. Vogelstein B, Kinzler KW. The genetic basis of human cancer. McGraw-Hill: New York, 1998.
33. Ebina Y, Okada S, Hamazaki S, *et al.* Nephrotoxicity and renal cell carcinoma after use of iron- and aluminum- nitrilotriacetate complexes in rats. J Natl Cancer Inst 1986;76:107–113.
34. Tanaka T, Iwasa Y, Kondo S, *et al.* High incidence of allelic loss on chromosome 5 and inactivation of $p15^{INK4B}$ and $p16^{INK4A}$ tumor suppressor genes in oxystress-induced renal cell carcinoma of rats. Oncogene 1999;18:3793–3797.
35. Hiroyasu M, Ozeki M, Kohda H, *et al.* Specific allelic loss of $p16^{INK4A}$ tumor suppressor gene after weeks of iron-mediated oxidative damage during rat renal carcinogenesis. Am J Pathol 2002;160: 419–424.
36. Toyokuni S, Uchida K, Okamoto K, *et al.* Formation of 4-hydroxy-2-nonenal-modified proteins in the renal proximal tubules of rats treated with a renal carcinogen, ferric nitrilotriacetate. Proc Natl Acad Sci USA 1994;91:2616–2620.
37. Toyokuni S, Mori T, Dizdaroglu M. DNA base modifications in renal chromatin of Wistar rats treated with a renal carcinogen, ferric nitrilotriacetate. Int J Cancer 1994;57:123–128.
38. Toyokuni S, Luo XP, Tanaka T, *et al.* Induction of a wide range of C_{2-12} aldehydes and C_{7-12} acyloins in the kidney of Wistar rats after treatment with a renal carcinogen, ferric nitrilotriacetate. Free Radic Biol Med 1997;22:1019–1027.
39. Kurokawa Y, Maekawa A, Takahashi M, *et al.* Toxicity and carcinogenicity of potassium bromate—a new renal carcinogen. Environ Health Perspect 1990;87:309–335.
40. Kasai H, Nishimura S, Kurokawa Y, *et al.* Oral administration of the renal carcinogen, potassium bromate, specifically produces 8-hydroxydeoxyguanosine in rat target organ DNA. Carcinogenesis 1987;8:1959–1961.
41. Steenken S. Purine bases, nucleosides, and nucleotides: aqueous solution redox chemistry and transformation reactions of their radical reactions and e^- and .OH adducts. Chem Rev 1989;89:503–520.
42. Dizdaroglu M. Chemical determination of free radical-induced damage to DNA. Free Radic Biol Med 1991;10:225–242.
43. Kondo S, Toyokuni S, Tanaka T, *et al.* Overexpression of the hOGG1 gene and high 8-hydroxy-2′-deoxyguanosine (8-OHdG) lyase activity in human colorectal carcinoma: regulation mechanism of the 8-OHdG level in DNA. Clin Cancer Res 2000;6:p1394–p1400.
44. Endo Y, Marusawa H, Kou T, *et al.* Activation-induced cytidine deaminase links between inflammation and the development of colitis-associated colorectal cancers. Gastroenterology 2008;135:889–898, 898.e881–883.
45. Matsumoto Y, Marusawa H, Kinoshita K, *et al.* Helicobacter pylori infection triggers aberrant expression of activation-induced cytidine deaminase in gastric epithelium. Nat Med 2007;13:470–476.

46. Pasqualucci L, Bhagat G, Jankovic M, *et al.* AID is required for germinal center-derived lymphomagenesis. Nat Genet 2008;40:108–112.
47. Preston D, Kusumi S, Tomonaga M, *et al.* Cancer incidence in atomic bomb survivors. Part III. Leukemia, lymphoma and multiple myeloma, 1950–1987. Radiat Res 1994;137:pS68–pS97.
48. Tanaka K, Arif M, Eguchi M, *et al.* Frequent allelic loss of the RB, D13S319 and D13S25 locus in myeloid malignancies with deletion/translocation at 13q14 of chromosome 13, but not in lymphoid malignancies. Leukemia 1999;13:1367–1373.
49. Ripolles L, Ortega M, Ortuno F, *et al.* Genetic abnormalities and clinical outcome in chronic lymphocytic leukemia. Cancer Genet Cytogenet 2006;171:57–64.
50. Maser R, Choudhury B, Campbell P, *et al.* Chromosomally unstable mouse tumours have genomic alterations similar to diverse human cancers. Nature 2007;447:966–971.
51. Toyokuni S, Sagripanti J-L. Association between 8-hydroxy-2′-deoxyguanosine formation and DNA strand breaks mediated by copper and iron. Free Radic Bio IMed 1996;20:859–864.
52. Toyokuni S. Reactive oxygen species-induced molecular damage and its application in pathology. Pathol Int 1999;49:91–102.
53. Robles S, Adami G. Agents that cause DNA double strand breaks lead to *p16 ^{INK4a}* enrichment and the premature senescence of normal fibroblasts. Oncogene 1998;16:1113–1123.
54. Akatsuka S, Aung TT, Dutta KK, *et al.* Contrasting genome-wide distribution of 8-hydroxyguanine and acrolein-modified adenine during oxidative stress-induced renal carcinogenesis. Am J Pathol 2006;169:1328–1342.
55. Illei P, Rusch V, Zakowski M, *et al.* Homozygous deletion of *CDKN2A* and codeletion of the methylthioadenosine phosphorylase gene in the majority of pleural mesotheliomas. Clin Cancer Res 2003;9:2108–2113.
56. Klossner J, Kivisaari J, Niinikoski J. Oxygen and carbon dioxide tensions in the abdominal cavity and colonic wall of the rabbit. Am J Surg 1974;127:711–715.
57. Olynyk J, Clarke S. Iron overload impairs pro-inflammatory cytokine responses by Kupffer cells. J Gastroenterol Hepatol 2001;16:438–444.
58. Wang N. The preformed stomas connecting the pleural cavity and the lymphatics in the parietal pleura. Am Rev Respir Dis 1975;111:12–20.
59. Muchmore A, Decker J. Uromodulin. An immunosuppressive 85-kilodalton glycoprotein isolated from human pregnancy urine is a high affinity ligand for recombinant interleukin 1 alpha. J Biol Chem 1986;261:13404–13407.
60. Sherblom A, Decker J, Muchmore A. The lectin-like interaction between recombinant tumor necrosis factor and uromodulin. J Biol Chem 1988;263:5418–5424.
61. Sandhu H, Dehnen W, Roller M, *et al.* mRNA expression patterns in different stages of asbestos-induced carcinogenesis in rats. Carcinogenesis 2000;21:1023–1029.
62. Pass H, Lott D, Lonardo F, *et al.* Asbestos exposure, pleural mesothelioma, and serum osteopontin levels. N Engl J Med 2005;353:1564–1573.
63. Park E, Thomas P, Johnson A, *et al.* Osteopontin levels in an asbestos-exposed population. Clin Cancer Res 2009;15:1362–1366.
64. Jongsma J, van ME, Vooijs M, *et al.* A conditional mouse model for malignant mesothelioma. Cancer Cell 2008;13:261–271.
65. Altomare D, Vaslet C, Skele K, *et al.* A mouse model recapitulating molecular features of human mesothelioma. Cancer Res 2005;65:8090–8095.

Published OnlineFirst June 22, 2010; DOI:10.1158/0008-5472.CAN-09-3497

Cancer Research

Tetraspanin CD151 Regulates Transforming Growth Factor β Signaling: Implication in Tumor Metastasis

Rafal Sadej, Hanna Romanska, Dean Kavanagh, et al.

Cancer Res 2010;70:6059-6070. Published OnlineFirst June 22, 2010.

Published OnlineFirst June 22, 2010; DOI:10.1158/0008-5472.CAN-09-3497

Tumor and Stem Cell Biology

Cancer Research

Tetraspanin CD151 Regulates Transforming Growth Factor β Signaling: Implication in Tumor Metastasis

Rafał Sadej[1], Hanna Romanska[1,2], Dean Kavanagh[3], Gouri Baldwin[1], Takashi Takahashi[4], Neena Kalia[3], and Fedor Berditchevski[1]

Abstract

Tetraspanin CD151 is associated with laminin-binding integrins and controls tumor cell migration and invasion. By analyzing responses of breast cancer cells to various growth factors, we showed that depletion of CD151 specifically attenuates transforming growth factor β1 (TGFβ1)–induced scattering and proliferation of breast cancer cells in three-dimensional Matrigel. CD151-dependent cell scattering requires its association with either α3β1 or α6 integrins, but it is independent of the recruitment of CD151 to tetraspanin-enriched microdomains. We also found that CD151 regulates the compartmentalization of TGF-β type I receptor (TβRI/ALK-5) and specifically controls the TGFβ1-induced activation of p38. In contrast, signaling leading to activation of Smad2/3, c-Akt, and Erk1/2 proteins was comparable in CD151(+) and CD151(−) cells. Attenuation of TGFβ1-induced responses correlated with reduced retention in the lung vascular bed, inhibition of pneumocyte-induced scattering of breast cancer cells in three-dimensional Matrigel, and decrease in experimental metastasis to the lungs. These results identify CD151 as a positive regulator of TGFβ1-initiated signaling and highlight the important role played by this tetraspanin in TGFβ1-induced breast cancer metastasis. *Cancer Res; 70(14); 6059–70. ©2010 AACR.*

Introduction

Tetraspanin protein CD151/Tspan24 is a member of a large family of four transmembrane domain proteins, which directly interacts with laminin-binding integrins (i.e., α3β1, α6β1/β4, and α7β1; refs. 1, 2). It affects their ligand-binding properties, thus regulating adhesion-dependent signaling and postadhesion events including cell migration (3). In addition, it has been shown that CD151 regulates the internalization of the associated integrins, a process that is integral to cell motility (4). Finally, we have recently reported that CD151 specifically affects glycosylation pattern of α3β1, and CD151-dependent differences in glycosylation of this integrin contribute to the modulatory activity of CD151 toward this integrin (5).

In addition to this CD151 regulates activity of laminin-binding integrins through tetraspanin-enriched microdomains (TERM or TEM), molecular aggregates on the plasma membrane, which include other tetraspanins and cytoplasmic signaling proteins (3). Association with CD151 is critical for the recruitment of laminin-binding integrins to TERM, where they can cooperate with other TERM-associated transmembrane proteins (6).

Cooperation between integrins and receptors to various growth and chemotactic factors is well established and occurs at multiple levels (7, 8). This involves cell type–specific association of various integrins with growth factor/chemokine receptors (GF-/ChR), integrin-mediated control over ligand-induced activation of GF-/ChR, and adhesion-dependent modulation of signaling pathways downstream of activated GF-/ChR. Integrin-associated transmembrane proteins including CD47, tetraspanins, and the L6-Ag family members can all function as mediators in communication between integrins and GF-/ChR (3, 9–11). We and others have previously described the association of tetraspanins with transmembrane receptors to growth factors including epidermal growth factor receptor (12, 13), receptor to hepatocyte growth factor (c-Met; ref. 14), and receptor for Steel factor (c-Kit; ref. 15). Furthermore, it has been proposed that tetraspanin microdomains may represent a focal point in which signaling through integrins and receptors for growth/chemotactic factors can be coordinated (3). Indeed, it has been shown that adhesion-dependent cellular responses triggered by activated c-Met are regulated by tetraspanins CD82 and CD151 (14, 16). Likewise, CD81 and CD9 regulated adhesion-dependent proliferation in response to fibroblast growth factor (17). In addition, tetraspanins may target growth factor receptors independent of their association with integrins (12, 14), and this may involve

Authors' Affiliations: [1]School of Cancer Sciences, [2]Department of Pathology, and [3]School of Clinical and Experimental Medicine, The University of Birmingham, Edgbaston, Birmingham, United Kingdom; and [4]Center for Neurological Diseases and Cancer, Nagoya University Graduate School of Medicine, Nagoya, Japan

Note: Supplementary data for this article are available at Cancer Research Online (http://cancerres.aacrjournals.org/).

Corresponding Author: Fedor Berditchevski, School of Cancer Sciences, The University of Birmingham, Edgbaston, Birmingham, B15 2TT, United Kingdom. Phone: 44-121-414-2801; Fax: 44-121-414-4486; E-mail: f.berditchevski@bham.ac.uk.

doi: 10.1158/0008-5472.CAN-09-3497

Published OnlineFirst June 22, 2010; DOI:10.1158/0008-5472.CAN-09-3497

tetraspanin-dependent changes in surface compartmentalization of the receptors (13, 18).

Here, we found that depletion of CD151 attenuated the responses of breast cancer cells to transforming growth factor β1 (TGFβ1) in three-dimensional extracellular matrix (ECM). This correlated with specific changes in the TGFβ1-induced signaling leading to the activation of p38. Importantly, we found that attenuated responses to TGFβ1 correlated with decreased retention of CD151-depleted cells in the lungs, inhibition of tumor cell growth and scattering in coculture with lung epithelial cells, and, consequently, diminished metastatic burden of breast cancer cells.

Materials and Methods

Cells, antibodies, and reagents

MDA-MB-231/CD151(+), MDA-MB-231/CD151(−), MDA-MB-231/CD81(−), MDA-MB-231/α3β1^{low}, MDA-MB-231/α6β4^{low}, DCIS.com/CD151(+), and DCIS.com/CD151(−) cell lines were generated using appropriate short hairpin RNA lentiviral constructs with cells expressing low levels of the target proteins being selected after cell sorting (5, 19, 20). MDA-MB-231/CD151rec, MDA-MB-231/CD151palm, and MDA-MB-231/CD151-QRD cell lines were established after the transfection of MDA-MB-231/CD151(−) cells with the wild-type and appropriate mutants of CD151 and subsequent selection CD151-expressing cells by cell sorting (5). Cell lines expressing low levels of α6 integrins (MDA-MB-231/α6^{low}β1/β4 and MDA-MB-231/α3β1^{low}α6^{low}β1/β4) were established by infecting of MDA-MB-231 and α3β1^{low} cells with pLVTHM-based lentivirus encoding short hairpin RNA that targets α6 integrin subunit (target sequence, 5′-GGUCGUGACAUGUGCUCAC-3′). To generate green fluorescent protein (GFP)–expressing cells, MDA-MB-231/CD151(+) and MDA-MB-231/CD151(−) were transduced with pLVTHM lentivirus (encoding GFP), which was produced in 293T cells using a standard protocol (20). All MDA-MB-231 and 293T cells were grown in DMEM (Sigma) supplemented with 10% fetal bovine serum (FBS). HPL1D cells (21) were cultured in Ham F12 media with 5 μg/mL insulin, 5 μg/mL transferrin, 10^{-7} mol/L hydrocortisone, 2×10^{-7} mol/L thyronine, and 1% of FBS. The mouse anti-CD151 monoclonal antibodies (mAb) used were 5C11 (22), 11B1G4 (provided by Dr. L. Ashman, University of Newcastle, Newcastle, Australia), and NCL-CD151 (Novocastra). Rabbit polyclonal antibodies against TGFβR1 were from Santa Cruz; mouse mAb against β-actin was from Sigma; and mouse mAb against β4 integrin subunit (3E1) was from Chemicon. Rabbit polyclonal antibodies to α3 and α6 integrin were generously provided by Dr. F. Watt (Cambridge Research Institute, Cambridge, UK) and Dr. A. Cress (Arizona Cancer Center, Tuscon, AZ). Mouse monoclonal to α3- (A3-IVA5), α6- (A6-ELE), and β1- (TS2/16) integrin subunit were previously described (23–25). The rest of the antibodies used in this study were purchased from Cell Signaling Technology. All growth factors were purchased from PeproTech. SB431542 was from Calbiochem.

Culturing cells in three-dimensional Matrigel

Cell culturing in three-dimensional Matrigel was previously described (20). In some experiments, cells were cultured in endothelial basal medium (Promocell), which was supplemented with 2% FBS and various growth factors/chemokines (at 10 ng/mL); growth medium was replaced every third day. To evaluate cell proliferation in three-dimensional Matrigel, AlamarBlue (Invitrogen) was added at different time points to the growth media and cells were further incubated for 4 hours at 37°C. Fluorescence of the samples was measured using the Fluoroskan plate reader. In cell coculture experiments, HPL1D cells were grown in 48-well plates until they reached 80% confluency: MDA-MB-231 cells suspended in Matrigel (8×10^3/200 μL) were subsequently overlaid and cultured for 7 to 10 days with growth media (DMEM/10%FCS) being replaced every third day. In some experiments, GFP-expressing MDA-MB-231 cells were premixed with HPL1D cells at the ratio 1:100 and incubated for 30 to 60 minutes on a slowly rocking platform to induce the formation of cell aggregates. Aggregates were carefully suspended in Matrigel and cultured for 7 to 10 days. For all three-dimensional culture experiments, representative pictures were taken every 2 to 3 days using the Nikon Eclipse TS100 microscope.

Analysis of TGFβ1-induced signaling

Cells spread on Matrigel-coated (10 μg/mL) culture plates were serum starved overnight and subsequently stimulated with 10 ng/mL TGFβ1 for different length of time. Cells were lysed in the ice-cold Laemmli buffer supplemented with 2 mmol/L phenylmethylsulfonyl fluoride, 10 μg/mL aprotinin, 10 μg/mL leupeptin, 100 mmol/L Na3VO4, 10 mmol/L NaF, and 10 mmol/L Na3P4O7. Proteins separated by SDS-PAGE were transferred onto nitrocellulose membrane and probed with various antibodies using a standard protocol.

Fractionation in sucrose gradient

Fractionation of cellular lysates in the gradient of sucrose was carried out as previously described (13, 18). In brief, cells were homogenized in 100 mmol/L Na_2CO_3 (pH 11.0) by passing through a 25G hypodermic needle, and the lysates were subsequently sonicated (4 × 20 s bursts, 1-min interval, power 20). The lysates were mixed with two volumes of 2 mol/L sucrose solution and overlaid with two sucrose solutions (35% and 5%). Samples were centrifuged at 100,000 *g* for 16 to 18 hours at 4°C in a Beckman SW60 rotor, and 10 equal volume fractions were collected from the top of gradient. The pellet was suspended in 200 μL of the lysis buffer. Equal amounts of each fraction were mixed with 4× Laemmli loading buffer, and the proteins were resolved by SDS-PAGE. Fractional distribution of proteins was subsequently analyzed by Western blotting.

Flow cytometry analysis

Cells were detached with enzyme-free cell dissociation buffer (Life Technologies) and kept for 1 hour on ice with saturating concentrations of appropriate mouse monoclonal antibodies. Staining was visualized using phycoerythrin-conjugated goat

Published OnlineFirst June 22, 2010; DOI:10.1158/0008-5472.CAN-09-3497

anti-mouse IgG antibodies, and samples were analyzed with COULTER Epics XL.

Metastasis experiments

All experiments were performed in accordance with institutional and national animal research guidelines. Cells were injected i.v. into the lateral tail vein of 4- to 5-week-old athymic mice to evaluate lung colonization. Mice were injected with 5×10^5 cells/150 μL PBS/mouse. Six to 10 animals per group were used in the experiments. The experiments were terminated 8 weeks postinjection (or earlier if mice with adverse symptoms were observed). At termination, the lungs were removed and fixed in 10% buffered formalin and processed for histologic and immunohistochemical analyses.

Histology and morphometry

Paraffin sections of formalin-fixed lungs were processed routinely for histology. The sections stained with H&E were analyzed, and images were captured using the Nikon E400 DS-U2/L2 software (Japan). For quantitative analysis, four sections at the distance of 200 μm on either side of the hilum were cut and immunostained for vimentin (DAKO) using a standard avidin-biotin-peroxidase complex method. Metastatic foci were counted in two low-power fields (4×) at each level, and their area was quantified using the AxioVision LE software (Zeiss). The numbers represent the average from eight counts per measurements. The mean ± SEM was calculated, and statistical analyses were carried out by the unpaired *t* test using a GraphPad Prism 3.2 program (GraphPad Software).

Analysis of tumor cell trafficking *in vivo* using intravital microscopy

Male C57BL/6 mice were anaesthetized with ketamine hydrochloride (100 mg/kg Vetalar; Amersham Biosciences and Upjohn Ltd.) and xylazine hydrochloride (10 mg/kg; Millpledge Pharmaceuticals). Animals subsequently underwent carotid artery cannulation to allow administration of cells fluorescently labeled with BCECF-AM (PPL 40/2749). Following laparotomy, the left hepatic lobe was exteriorized and visualized intravitally using an inverted fluorescent microscope (Olympus). MDA-MB-231/CD151(+) or MDA-MB-231/CD151(−) (1×10^6) cells were administered in a 100-μL bolus through the carotid artery. Seven fields of view containing a postsinusoidal venule and surrounding sinusoidal capillaries were analyzed 1 hour postinjection of cells. Lung tissue was isolated from sacrificed mice at the end of the intravital experiments. Tissue was washed in 0.9% saline and also analyzed on the inverted fluorescent microscope. Ten fields of view were selected in a set pattern, and adherent cells were counted. The average from these 10 fields was obtained from each of the five separate experiments.

Results

Depletion of CD151 affects the responses of breast cancer cells to TGFβ1

We have analyzed whether the absence of CD151 can affect responses of breast cancer cells to various growth factors and chemokines. Initially, we used MDA-MB-231/CD151(+) and MDA-MB-231/CD151(−) cells, and assessed the growth of these cells in three-dimensional Matrigel. In agreement with the previous studies, we found that depletion of CD151 did not affect surface expression of predominant integrins in MDA-MB-231 cells (Supplementary Fig. S1). Ten growth/chemotactic factors were analyzed in these experiments including PDGF-BB, HB-EGF, EGF, bFGF, SDF-1, TGFα, HGF, TGFβ1, IGF-I, and IL-1. Under the control conditions (i.e., in the absence of additional growth factors), both MDA-MB-231/CD151(+) and MDA-MB-231/CD151(−) cells formed compact round aggregates (Fig. 1A, top). The morphologic appearance of colonies was not affected when cells were cultured in the presence of HGF, IL-1, EGF, IGF-I, PDGF-BB, SDF1, HB-EGF, and TGFα (Supplementary Fig. S2 and results are not shown). Tight intercellular interactions within aggregates were looser in the presence of bFGF, but we observed no apparent difference between the CD151(+) and CD151(−) cells (Supplementary Fig. S2). By contrast, the CD151-dependent differential response was seen when cells were grown in the presence of TGFβ1. While <20% of CD151-positive aggregates retained compact morphology, the majority of colonies appeared as aggregates of loosely associated cells, some of which developed characteristic thin protrusions (thereafter, we referred to this type of colony as having a "scattered" phenotype; Fig. 1A, bottom left). Short protrusions were first observed 4 days after cells were seeded in Matrigel, and they gradually became more prominent after 8 days in three-dimensional culture (Fig. 1B). In contrast to CD151-positive cells, ~80% of MDA-MB-231/CD151(−) colonies remained compact and had smooth contours during the time course of the experiments (Fig. 1A, bottom right, and C). Although there was no obvious difference between CD151-positive and CD151-negative cells in the number of colonies formed in the presence of TGFβ1, the proliferative rate of MDA-MB-231/CD151(−) cells appeared to be consistently lower (Fig. 1D). Similarly, TGFβ1-induced proliferation of another breast cancer cell line (DCIS.com) was also attenuated after depletion of CD151 (Supplementary Fig. S3). Importantly, the effect of CD151 depletion on TGFβ1-induced signaling was specific as knockdown of tetraspanin CD81 did not change responses of MDA-MB-231 cells (Supplementary Fig. S4). These data showed that CD151 specifically regulates TGFβ1-induced responses of breast cancer cells in three-dimensional Matrigel.

The role of CD151-associated integrins and tetraspanin microdomains in regulating cellular responses to TGFβ1

We and others have previously reported that in MDA-MB-231 cells, the function of CD151 is closely linked to laminin-binding integrins (i.e., α3β1, α6β1, and α6β4; refs. 5, 20, 26). To examine the involvement of these integrins in CD151-dependent scattering induced by TGFβ1, we initially examined the responses of MDA-MB-231/CD151-QRD cells (5). These cells were derivative of MDA-MB-231/CD151(−) line, and they expressed the mutant of CD151 deficient in its ability to form complexes with integrins (5). As illustrated

Published OnlineFirst June 22, 2010; DOI:10.1158/0008-5472.CAN-09-3497

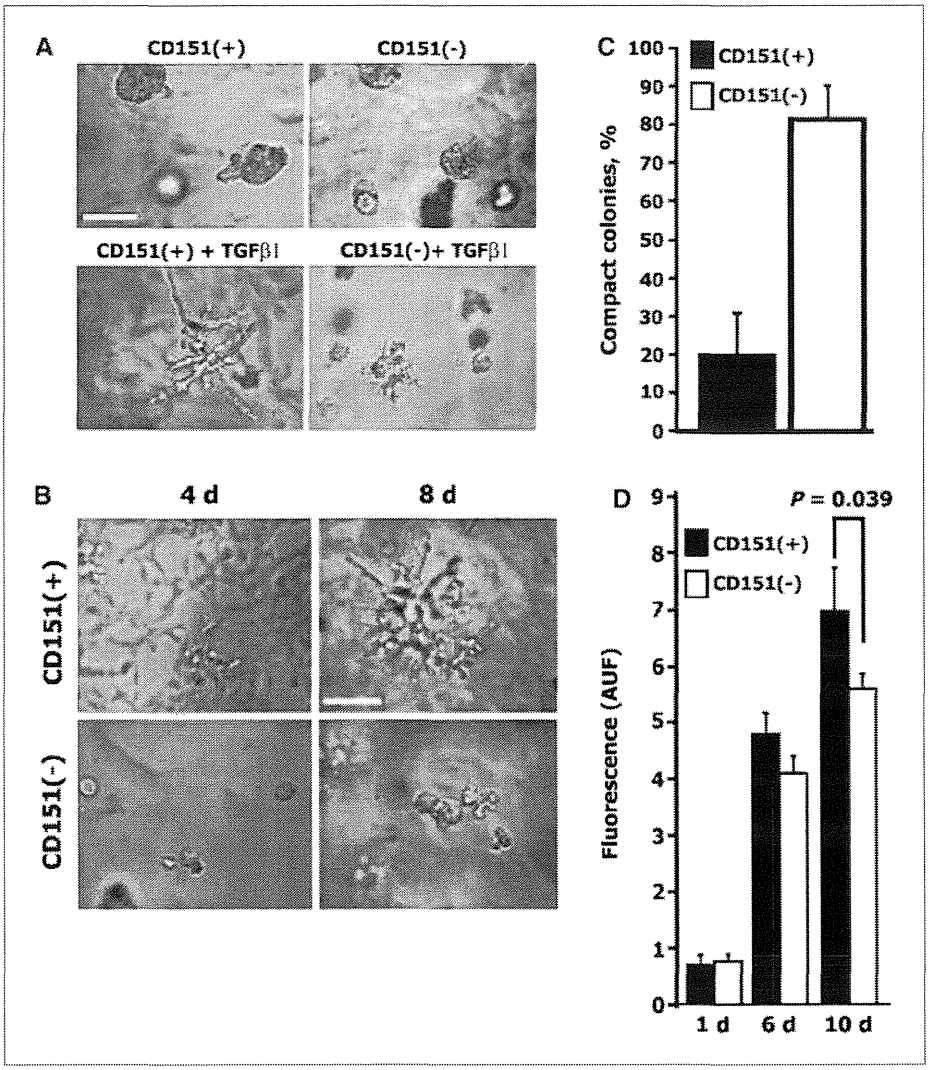

Figure 1. CD151 regulates responses of MDA-MB-231 breast cancer cells to TGFβ1. A and B, cells were embedded into growth factor–reduced Matrigel as described in Materials and Methods and grown for 8 d without (top) or in the presence of TGFβ1 (10 ng/mL). Presented photographs of representative fields. Scale bar, 50 μm. B, the time course of cellular responses to TGFβ1 in Matrigel. Growth of cells in three-dimensional Matrigel was analyzed as described in A. Scale bar, 50 μm. C, quantification of TGFβ1-induced changes in morphology of the colonies in three-dimensional Matrigel. More than 50 colonies were analyzed for each of the cell lines in each of three separate experiments. Colonies were defined as having a "compact phenotype" when no individual cell borders could be discerned within the colony. Ratio of average number of "compact" colonies for CD151-positive and CD151-depleted MDA-MB-231 was calculated for each experiment. Columns, mean of ratios; bars, SD. D, measurements of cell proliferation in the presence of TGFβ1. Cell proliferation was measured using Alamar Blue by a spectrofluorometric method. Columns, mean of three experiments (each in triplicate); bars, SD. AFU, arbitrary fluorescence units.

in Fig. 2, the response of MDA-MB-231/CD151-QRD cells was comparable with that of the CD151-negative cells with ~90% of all colonies remaining compact in the presence of TGFβ1. By contrast, the response to TGFβ1 was restored when MDA-MB-231/CD151(-) cells were reconstituted with the wild-type CD151 (Fig. 2A and B). Flow cytometry experiments have shown that CD151-QRD and CD151wt proteins expressed at the comparable levels on the surface of reconstituted MDA-MB-231 cells (Supplementary Table S1). We next investigated which of the laminin-binding integrins contribute to CD151-dependent responses of MDA-MB-231 cells to TGFβ1. To this end, we have generated two new cell lines: MDA-MB-231/α6β1/$\beta4^{low}$, deficient in expression of both α6 integrins (i.e., α6β1 and α6β4), and MDA-MB-231/α3$\beta1^{low}$α6 β1/$\beta4^{low}$, deficient in expression of all laminin-binding integrins (Supplementary Fig. S1A). In these experiments, we also used α3β1-deficient cells (MDA-MB-231/α3$\beta1^{low}$; ref. 20). Surprisingly, both MDA-MB-231/α3$\beta1^{low}$ and MDA-MB-231/α6β1/$\beta4^{low}$ cells were able to form colonies with characteristic scattered appearance, and only deficiency in all CD151-associated integrins completely abolished responses to TGFβ1 (Supplementary Fig. S5; Fig. 2C). These results confirmed that the modulatory activity of CD151 requires its association with integrins and suggested functional redundancy of various CD151-integrin complexes in TGFβ1-induced scattering. Palmitoylation-dependent recruitment of the proteins to tetraspanin-enriched microdomains is critical for many of the tetraspanin activities (27). To investigate whether palmitoylation of CD151 is necessary for TGFβ1-induced responses, we analyzed the behavior of MDA-MB-231/CD151palm(-) cells. As illustrated in Fig. 2D, expression of palmitoylation-deficient CD151 in MDA-MB-231/CD151 (-) fully restored the ability of the cells to form scattered colonies in the presence of TGFβ1. These results indicated that the association with other tetraspanins (and recruitment to tetraspanin microdomains) was not essential for CD151-dependent cellular responses to this cytokine.

Published OnlineFirst June 22, 2010; DOI:10.1158/0008-5472.CAN-09-3497

The effect of CD151 depletion on TGFβ1-induced signaling

Pleiotropic effects of TGFβ1 on cell behavior is mediated by Smad proteins, which function as transcriptional modulators, and through activation of several Smad-independent signaling pathways involving P13-K, Erk1/2, and p38 kinases (28). To analyze how depletion of CD151 affects TGFβ1-induced signaling, we assessed phosphorylation of various TGFβ1 targets in cells plated on Matrigel under serum-free conditions and subsequently stimulated with the cytokine for various time intervals. As expected, incubation with TGFβ1 resulted in the phosphorylation of Smad2 and Smad3: the phosphorylation levels of the proteins peaked at 1 hour after the stimulation and then decreased to undetectable levels by 12 hours (Fig. 3A and B). We observed no difference between CD151-positive and CD151-negative cells in the kinetics and degree of phosphorylation of Smad2/3 proteins in these experiments (Fig. 3A and B). Thus, it seemed that CD151 does not influence Smad-dependent signaling pathway. Similarly, phosphorylation levels of Erk1/2 and c-Akt were comparable at all analyzed time points (data not shown; Fig. 3A and B). By contrast, there was a consistent difference in TGFβ1-induced phosphorylation of p38. In MDA-MB-231/CD151(+) cells, after the initial sharp increase (~4-fold increase), the level of phospho-p38 has returned to its basal level (i.e., 0 time point) by 48 hours. On the other hand, the degree of TGFβ1-induced phosphorylation of p38 in CD151-negative MDA-MB-231 cells was significantly lower when compared with nonstimulated cells, with maximal ~1.5-fold increase by 1 hour (Fig. 3A and C). Furthermore, p38 phosphorylation was sustained at almost the same level for up to 48 hours. A specific CD151-dependent effect on TGFβ1-induced phosphorylation of p38 was also observed

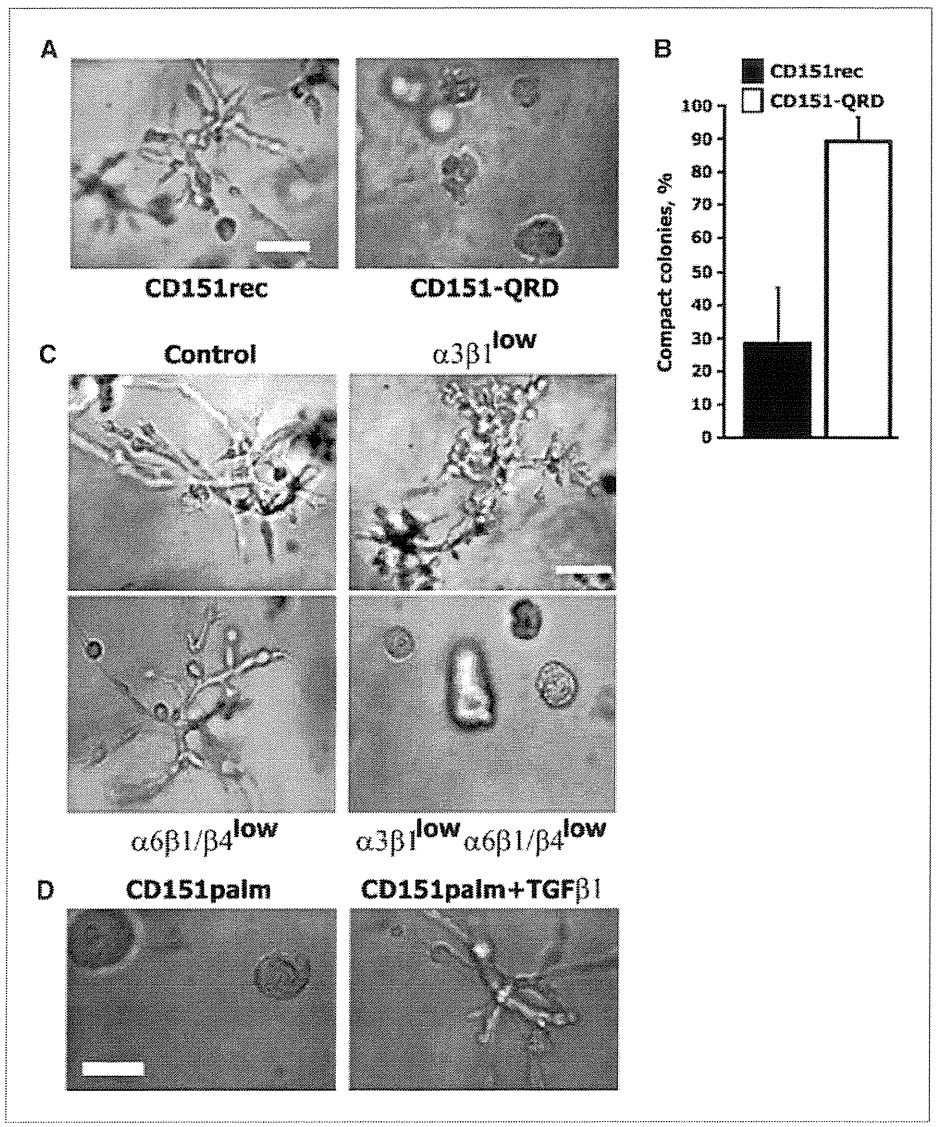

Figure 2. The association with integrins is critical for CD151-dependent cellular responses to TGFβ1. Growth of cells in three-dimensional Matrigel (A) and quantification of cellular responses (B) were performed as described in the legend of Fig. 1. C and D, MDA-MB-231, MDA-MB-231/CD151rec, MDA-MB-231/CD151-QRD, MDA-MB-231/CD151palm, MDA-MB-231/$\alpha3\beta1^{low}$, MDA-MB-231/$\alpha6^{low}\beta1/\beta4$, and MDA-MB-231/$\alpha3\beta1^{low}\alpha6^{low}\beta1/\beta4$ cells were plated in three-dimensional Matrigel and grown in presence of TGFβ1 as described in Fig. 1. Scale bar, 50 μm.

Published OnlineFirst June 22, 2010; DOI:10.1158/0008-5472.CAN-09-3497

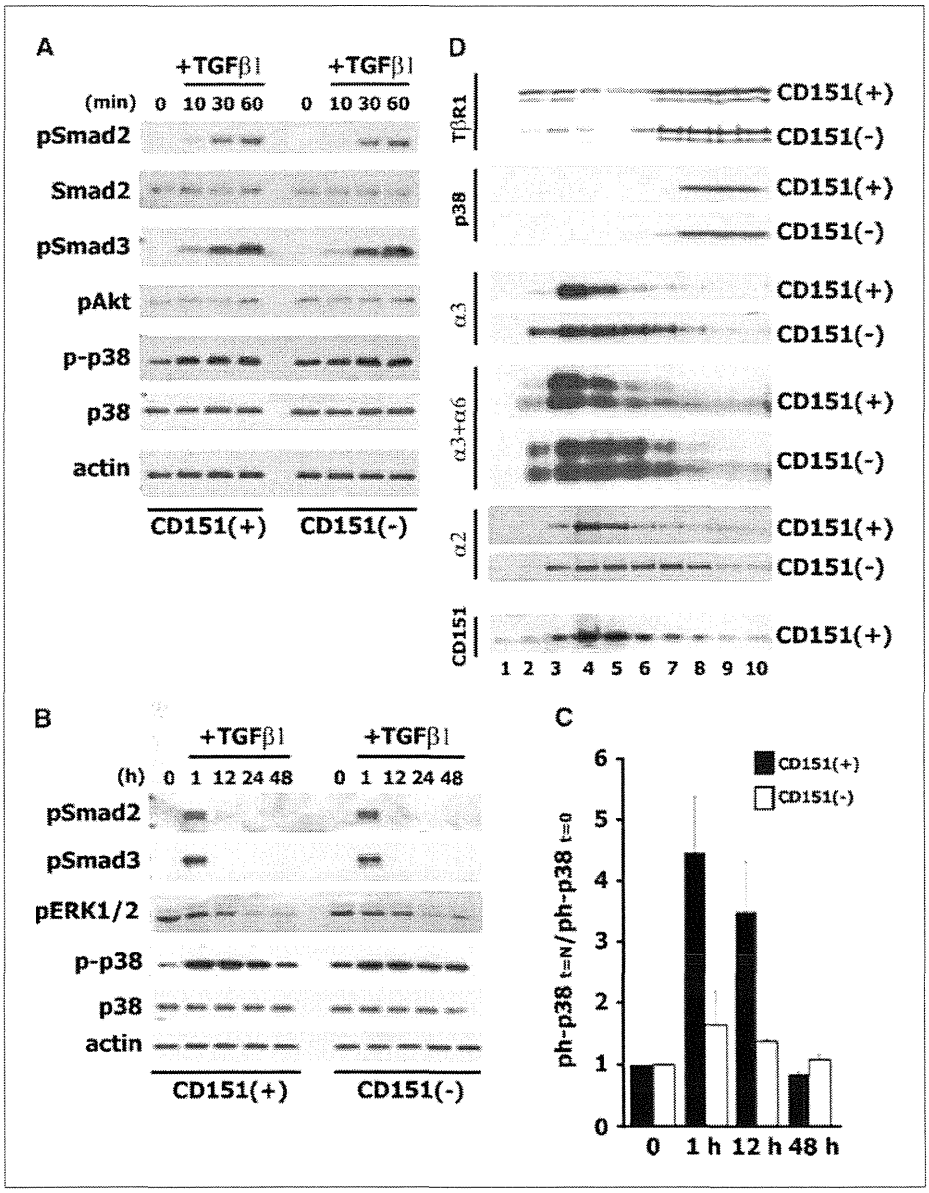

Figure 3. The effect of CD151 depletion on TGFβ1-induced signaling. A and B, serum-starved MDA-MB-231/CD151(+) and MDA-MB-231/CD151(–) cells were incubated with TGFβ1 (10 ng/mL) for indicated time intervals and then scraped into Laemmli buffer. Proteins were resolved in 10% SDS-PAGE under reduced conditions. The proteins were transferred to a nitrocellulose membrane and probed with indicated antibodies. C, densitometric analysis of activation p38 (i.e., measurements of phospho-p38) for the results shown in B. Measurements were done for three independent experiments. A.D.U., arbitrary densitometry units. D, the role of CD151 in the membrane compartmentalization of TβRI. Cell lysates from MDA-MB-231/CD151 (+) and MDA-MB-231/CD151(–) were fractionated in gradient of sucrose as described in Materials and Methods. Equal volumes of each fraction were resolved in 10% SDS-PAGE. Distribution of proteins in the gradient fractions was assessed by Western blotting using specific antibody Abs. The α2, α3, and α6 panels represent Western blots detecting corresponding integrin subunits.

in DCIS.com cells (Supplementary Fig. S6). These results showed that CD151 deficiency resulted in specific alterations in TGFβ1-induced signaling. It has been recently reported that TGFβ1-induced activation of p38 was influenced by cholesterol-dependent redistribution of TGF-β type I receptor (TβRI/ALK-5) on the plasma membrane (29). Fractionation in sucrose gradient was used to examine whether the effect of CD151 on p38 activation also involves changes in the membrane compartmentalization of TβRI/ALK-5. Although the major pool of TβRI/ALK-5 molecules was found in the heavy fractions of sucrose gradient, a significant proportion of the receptor was floating in the light fractions (Fig. 3D). Importantly, we have consistently observed (three independent experiments) that depletion of CD151 in MDA-MB-231 cells resulted in the decrease in the proportion of TβRI/ALK-5 in the light fraction of the gradient. Control experiments have shown that the total cellular levels of TβRI/ALK-5 were comparable in CD151(+) and CD151(–) cells (Supplementary Fig. S7). By contrast, fractional distribution of CD151 and the associated integrins was different with most of the signal detected in the fractions 3 to 6 (Fig. 3D). Furthermore, depletion of CD151 resulted in the redistribution of α3β1 in sucrose gradient fractions. In additional experiments, we found no evidence for the interaction between CD151 and TβRI/ALK-5 (data not shown).

Depletion of CD151 attenuates pulmonary metastasis of breast cancer cells

It has been reported that TGFβ1 plays a critical role in pulmonary metastasis of MDA-MB-231 (30). Thus, we used